

Non-stabilizerness in kinetically-constrained Rydberg atom arrays

Ryan Smith,¹ Zlatko Papić,¹ and Andrew Hallam¹

¹*School of Physics and Astronomy, University of Leeds, Leeds LS2 9JT, UK*

(Dated: June 21, 2024)

Non-stabilizer states are a fundamental resource for universal quantum computation. However, despite broad significance in quantum computing, the emergence of “many-body” non-stabilizerness in interacting quantum systems remains poorly understood due to its analytical intractability. Here we show that Rydberg atom arrays provide a natural reservoir of non-stabilizerness that extends beyond single qubits and arises from quantum correlations engendered by the Rydberg blockade. We demonstrate that this non-stabilizerness can be experimentally accessed in two complementary ways, either by performing quench dynamics or via adiabatic ground state preparation. Using the analytical framework based on matrix product states, we explain the origin of Rydberg non-stabilizerness via a quantum circuit decomposition of the wave function.

Introduction.—Concepts from quantum information theory have become indispensable tools for understanding many-body quantum systems. For example, quantum entanglement is now central to the understanding of topological order [1–4] and non-equilibrium dynamics of interacting quantum systems [5–8] (see Ref. [9] for a review). Moreover, low-energy eigenstates of quantum Hamiltonians typically have a limited amount of entanglement, making them amenable to variational ansätze such as tensor networks [10, 11], which underpin powerful numerical algorithms such as the density-matrix renormalization group (DMRG) [12].

Entanglement, however, is not the only resource required for large-scale quantum computation. The implementation of a universal set of gates is a major challenge – typically only the Clifford group of multi-qubit Pauli gates is feasible, a set of gates that can be efficiently simulated classically [13, 14]. One approach to universal quantum computation is to inject non-stabilizer or “magic” states into the circuit [15–17]. From a practical standpoint, this raises the question how such special states can be conveniently generated. While there has been much progress in understanding the non-stabilizerness of *few-qubit* systems [16, 18], analogous property in *many-qubit* Hamiltonian and circuit systems is a subject of active investigation [19–29]. Consequently, many basic questions remain open, e.g., whether non-stabilizerness can play a similar role to entanglement in characterizing the properties of many-body systems.

Unfortunately, quantifying the non-stabilizerness of generic wave functions is very costly. In this work we focus on the Stabilizer Rényi Entropy (SRE) [22, 30], which has recently been proposed as a measure of non-stabilizerness for many-qubit wave functions (we note there are related local measures such as “robustness of magic” [18, 31, 32] and Mana entropies for qudit systems [33, 34]). The SRE, while still exponentially hard to evaluate in general, can be approximated via Monte Carlo methods [24, 35, 36]. Moreover, for a class of matrix product states (MPS) with a low bond dimension, the SRE can be expressed in closed form [23, 37, 38].

Nevertheless, it remains unclear what information about the wave function is contained in its SRE. The studies of quantum spin chains and related models have empirically found that many-body ground states can exhibit varying levels of non-stabilizerness but generally do not approach the upper bound of the SRE, even at quantum critical points [24]. Thus, it is important to identify analytically tractable models where enhancement of SRE compared to a single qubit can be analytically understood.

In this work we study non-stabilizerness in the PXP model, an effective model of Rydberg atom quantum simulators [39–41]. This system gives rise to quantum many-body-scars (QMBSs) [42–45], a semiclassical dynamical effect which can be accurately described using a manifold of low-bond dimension MPS states [46, 47]. We analytically calculate the SRE across the MPS manifold associated with semiclassical dynamics of the PXP model, finding that the manifold hosts regions of large non-stabilizerness. The non-stabilizerness can be understood microscopically from the properties of the corresponding unitary circuit that generates the states in the manifold. Finally, we demonstrate that the MPS manifold is relevant for the physics of the full Rydberg model realized in experiment, and we propose two protocols that can be used to access the non-stabilizer states, either by performing the global quench or by adiabatically preparing the ground state by modulating the radius of the Rydberg blockade and chemical potential.

Stabilizer Rényi entropy of MPS states.—A useful measure of non-stabilizerness is the stabilizer Rényi entropy (SRE) of order n [22]:

$$m^{(n)}(|\psi\rangle) = (1 - n)^{-1} \ln \sum_{P \in \mathcal{P}_N} \frac{\langle \psi | P | \psi \rangle^{2n}}{2^N}, \quad (1)$$

where $|\psi\rangle$ is a pure state of N spins- $\frac{1}{2}$ and \mathcal{P}_N is the set of all N -strings of Pauli matrices $\{\sigma^\alpha\} = \{\mathbb{1}, \sigma^x, \sigma^y, \sigma^z\}$. The SRE is zero iff $|\psi\rangle$ is a stabilizer, it is invariant under Clifford unitaries and additive under tensor product [22].

The cost of directly evaluating Eq. (1) scales as 4^N , which rapidly becomes intractable. Instead, the SRE can

be approximated by Monte Carlo sampling over Pauli strings [24, 35], which scales more favorably but may require many samples for accurate statistics. Finally, the SRE can be calculated directly using MPS techniques, although with costly χ^{6n} scaling in the bond-dimension χ of the MPS [23]. We utilize the latter approach in this work as we focus on low- χ MPS states for which we can obtain analytical insight into the SRE.

We consider a translation-invariant MPS state $|\psi(A)\rangle$, defined on an infinite lattice with $d=2$ -dimensional local Hilbert space, $|\psi(A)\rangle = \sum_{\{\sigma_j\}} \text{tr}(\cdots A^{\sigma_{j-1}} A^{\sigma_j} A^{\sigma_{j+1}} \cdots) |\{\sigma_j\}\rangle$, where A_j^σ is a set of d matrices of dimensions $\chi \times \chi$, with χ being the MPS bond-dimension. To calculate the SRE of $|\psi(A)\rangle$, we employ the replica trick method introduced in Ref [23].

Let us denote by $B_{i,j}^{\sigma^s} = (A_{i,j}^\sigma)^{\otimes 2n}$ a $2n$ -fold copy of A and the tensor $\Lambda^{(n)} = (1/2) \sum_{\alpha=0}^3 (\sigma_j^\alpha)^{\otimes 2n}$. The SRE in the thermodynamic limit is obtained from the modified $\chi^{4n} \times \chi^{4n}$ transfer matrix:

$$\tau_{(ik),(jl)} = \sum_{s,s'} B_{i,j}^{\sigma^s} (\Lambda_1^{(n)} \otimes \cdots \otimes \Lambda_N^{(n)})^{\sigma^s, \sigma^{s'}} \bar{B}_{k,l}^{\sigma^{s'}}, \quad (2)$$

see Supplementary Material (SM) [48] for details. Denoting the dominant eigenvalue of τ as $\lambda_0^{(n)}$, the SRE is given by $m^{(n)}(|\psi(A)\rangle) = (1-n)^{-1} \ln \lambda_0^{(n)}$. As defined here, the SRE is an intensive quantity and it is upper-bounded by $m^{(n)} \leq (1/N) \ln \mathcal{D}$, where \mathcal{D} is the Hilbert space dimension [22].

PXP Model.—We focus on the kinetically constrained spin-1/2 PXP model [40, 49, 50]:

$$H_{\text{PXP}} = \frac{\Omega}{2} \sum_{j=1}^N P_{j-1} \sigma_j^x P_{j+1}, \quad (3)$$

where $\Omega=1$ is the Rabi frequency, N is the number of spins, and $P_j = (1 - \sigma_j^z)/2$ is the projector on the $|0\rangle$ state. With open boundary conditions we set $P_0 = P_{N+1} = \mathbb{1}$. The PXP model describes the low-energy physics of systems with the Rydberg blockade [51], a phenomenon where neighboring excitations of Rydberg atoms, e.g., states such as $|\dots 111 \dots\rangle$, are energetically forbidden. The blockade is imposed globally with the projector $\mathcal{P} = \bigotimes_j (\mathbb{1} - |11\rangle\langle 11|_{j,j+1})$ or, equivalently, in the local form using the P_j operators as in Eq. (3).

The PXP model is chaotic [40], and for typical initial states such as $|0\rangle = |0000\dots\rangle$, rapid thermalization is observed [39]. Nevertheless, the PXP model also hosts a small number of non-thermal QMBS eigenstates which are evenly distributed in energy and possess anomalously low entanglement entropy [40, 41, 52–57]. These “scarred” eigenstates have a high overlap with the $|\mathbb{Z}_2\rangle = |0101\dots\rangle$ state, leading to a suppressed growth of entanglement entropy and periodic revivals in local observables [39]. This dynamics has an elegant explanation

in terms of low- χ MPS states [46], which will allow us to gain analytical insight into the out-of-equilibrium behavior of non-stabilizerness in this interacting model.

The dynamics of SRE when the PXP model is quenched from $|0\rangle$ and $|\mathbb{Z}_2\rangle$ initial states is presented in Fig.1(a). We obtain the time-evolved state in MPS representation for various bond dimensions using a numerical implementation of the time-dependent variational principle (TDVP) [58] and then evaluate its SRE from Eq. (2). For the scarred $|\mathbb{Z}_2\rangle$ state, we see a complex dynamics of SRE, with a single large peak in between two smaller peaks. This data is well-converged already with small χ . The complex dynamics of SRE should be compared with simple spin precession generated by $H = \sum_j \sigma_j^x/2$, which is also shown in Fig.1(a). By contrast, the thermalizing $|0\rangle$ state displays a rapid increase in SRE exceeding the values reached from the $|\mathbb{Z}_2\rangle$ state. Following this initial increase, the SRE remains relatively stable despite increasing entanglement entropy [40].

Since non-stabilizerness is a fundamentally basis dependent quantity, we emphasize that *a priori* it not clear if the behavior seen in Fig.1(a) is truly a many-body phenomenon or if it can be removed through a local unitary rotation. In SM [48] we minimized the SRE over local unitary rotations, confirming that large SRE in the $|0\rangle$ case cannot be generated by single-qubit rotations. Next we explain how this many-body effect can be understood within MPS framework.

Non-stabilizerness of MPS ansatz.— The short-time dynamics of the PXP model can be understood semiclassically using a low- χ MPS ansatz [46, 47]. The ansatz is obtained by applying the Rydberg blockade projector \mathcal{P} to a product of spin coherent states, $|\psi(\boldsymbol{\theta}, \boldsymbol{\phi})\rangle = \mathcal{P} \bigotimes_j [\cos(\theta_j/2)|0\rangle_j - ie^{i\phi_j} \sin(\theta_j/2)|1\rangle_j]$, where θ_j, ϕ_j are the Bloch sphere angles of j th spin.

The state $|\psi(\boldsymbol{\theta}, \boldsymbol{\phi})\rangle$ can be equivalently expressed as a $\chi=2$ MPS [46]:

$$A^0(\theta_j, \phi_j) = \begin{pmatrix} \cos(\theta_j/2) & 0 \\ \sin(\theta_j/2) & 0 \end{pmatrix}, A^1(\theta_j, \phi_j) = \begin{pmatrix} 0 & -ie^{i\phi_j} \\ 0 & 0 \end{pmatrix}, \quad (4)$$

which defines a continuous manifold of states $\mathcal{M} = \text{span}\{|\psi(A)\rangle | \forall \theta_j, \phi_j\}$. As we are primarily interested in $|0\rangle$ and $|\mathbb{Z}_2\rangle$ initial states, we assume two-site periodicity of the angles, leaving the angles on even and odd sites, (θ_e, ϕ_e) and (θ_o, ϕ_o) , as our only parameters. Quantum dynamics can then be projected to \mathcal{M} using TDVP, resulting in a system of two non-linear differential equations for the angles, see [46] and SM [48].

The projection of dynamics into \mathcal{M} leads to perfectly periodic evolution of the SRE when starting in the $|\mathbb{Z}_2\rangle$ state, see Fig.1(b). Although the full dynamics in Fig.1(a) is not exactly periodic, the TDVP representation of $m^{(2)}$ within \mathcal{M} still shows excellent agreement. In particular, the distinctive pattern of a large peak surrounded by two smaller peaks in $m^{(2)}$ is fully reproduced

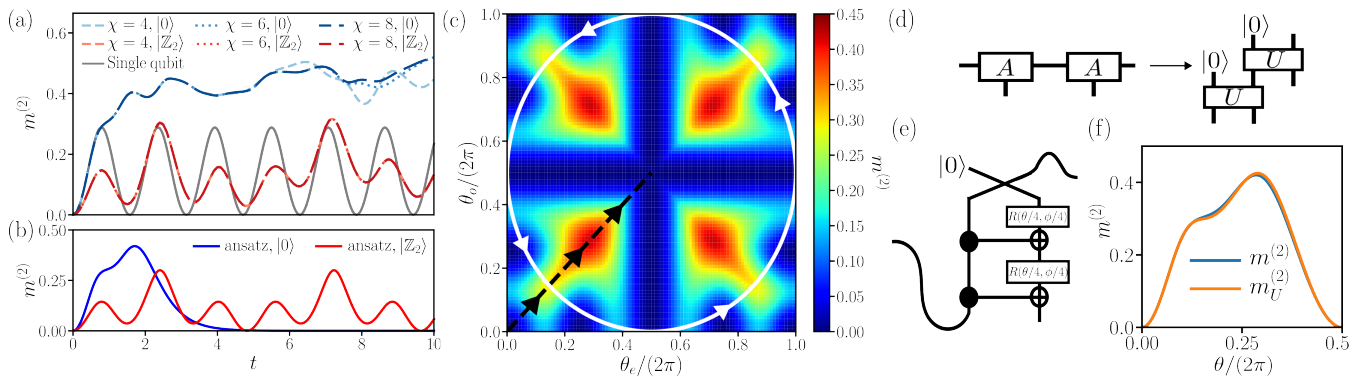


Figure 1. (a): The dynamics of $m^{(2)}$ following the quench from the $|0\rangle$ and $|\mathbb{Z}_2\rangle$ initial states in the PXP model with $N=51$ spins. Data is obtained numerically using TDVP for different bond dimensions χ indicated in the legend. Single qubit precession is shown in gray for comparison. (b): Same as (a) but the SRE is obtained analytically by integrating the equations of motions in the $\chi=2$ MPS manifold \mathcal{M} defined in Eq. (4). (c): Phase diagram of non-stabilizerness across the MPS manifold \mathcal{M} , plotted as a function of θ_e and θ_o angles. The trajectories traversed by the $|\mathbb{Z}_2\rangle$ and $|0\rangle$ states are shown by solid white and black dashed lines, respectively. (d)-(e): Decomposing the MPS tensors into unitary rotations (d), with the resulting PXP unitary circuit shown in (e). (f): $m^{(2)}$ of the MPS ansatz along the $|0\rangle$ trajectory is well-described by $m_U^{(2)}$, the non-stabilizerness of the input state ρ_{in} after being acted on by the unitary generated by the ansatz.

within \mathcal{M} , and we will provide its explanation below. For the $|0\rangle$ initial state, however, the agreement between full dynamics and \mathcal{M} is only good up to times $t \approx 1.5$, after which the TDVP clearly no longer captures the full SRE dynamics. This is expected due to the large leakage of the dynamics outside the manifold [46]. In fact, at late times the evolution of the $|0\rangle$ state becomes perpendicular to the ansatz and $m^{(2)}$ is stuck near zero. Nevertheless, comparing Fig.1(a) and Fig.1(b), we see that projection into \mathcal{M} captures well the early-time enhancement of the SRE, which will be our main focus below.

Fig.1(c) shows the SRE across the manifold \mathcal{M} plotted as a function of θ_e and θ_o angles. When either of the angles is zero, the MPS ansatz reduces to a simple product state, with one of the spins fixed to $|0\rangle$ and the other rotating in the xz -plane. Hence, the SRE reaches a maximum whenever it is furthest from the other spin being an σ^x or σ^z eigenstate, i.e., at $\theta_{o/e} = \pi/4, 3\pi/4, \dots$. Cases $\theta_{o/e} = \pi$ are also easy to understand, since one of the sites in the unit cell is guaranteed to be occupied, hence the other must be unoccupied due to the Rydberg blockade. Since this corresponds to the $|\mathbb{Z}_2\rangle$ product state, the SRE is zero along these lines. The non-trivial feature of the diagram in Fig.1(c) are the four arrow-like structures pointing towards the center. The SRE maxima lie at the centers of these arrows along the $\theta_e = \pm\theta_o$ line with a large value of $m^{(2)} \approx 0.42$, considerably larger than the quantum Ising model at its critical point [24, 36].

The TDVP trajectory followed by the $|\mathbb{Z}_2\rangle$ state in \mathcal{M} is shown by a white solid line in Fig. 1(c), moving periodically between high and low SRE regions. By contrast, the $|0\rangle$ state follows the black dashed line in Fig. 1(c), moving diagonally from $(\theta_o, \theta_e) = (0, 0)$ to $(\theta_o, \theta_e) = (\pi, \pi)$, passing through the state with maximal SRE before ex-

iting the manifold. Recalling Fig. 1(b), it is clear that the repeating pattern of three SRE peaks is due to the $|\mathbb{Z}_2\rangle$ trajectory cutting through the arrow-shaped regions in Fig. 1(c). The two smaller peaks in the SRE are from the sides of the arrow shape, suggesting they arise due to local non-stabilizerness, whereas the larger peak is a many-body effect. By contrast, the dynamics initialized in the $|0\rangle$ state directly flows towards the global non-stabilizerness maximum $m^{(2)} \approx 0.42$ within \mathcal{M} , close to the value in the full model in Fig. 1(a).

Thus, high non-stabilizerness is created under PXP dynamics within \mathcal{M} given that SRE is upper-bounded by $m^{(2)} \lesssim 0.48$, since the PXP Hilbert space dimension is given by the Fibonacci number [41].

The origin of non-stabilizerness.—To provide an intuitive understanding of large SRE in Fig. 1(c), we utilize a quantum circuit description. Any MPS can be rewritten so it satisfies the condition $\sum_{\sigma} (A^{\sigma})^{\dagger} A^{\sigma} = \mathbb{1}_{\chi}$ [10, 59] and we can think of it as χ columns of a $d\chi \times d\chi$ unitary matrix. The product structure of the MPS wave function $\dots A^{\sigma_j} A^{\sigma_{j+1}} \dots$ is reproduced by composing these unitary matrices in a staircase pattern as shown in Fig. 1(d), with one leg contracted with a dummy state $|0\rangle$ to select the first χ columns of the unitary. The ansatz described in Eq. (4) is no exception, it can be constructed from the two-qubit unitary given in Fig. 1(e):

$$U_{\text{MPS}} = \text{CNOT} R_{\theta/4, \phi/4}^{(2)} \text{CNOT} R_{\theta/4, \phi/4}^{(2)} \text{SWAP}, \quad (5)$$

where $R_{\theta, \phi}^{(2)} = \exp(i(\pi/2)\mathbf{n} \cdot \boldsymbol{\sigma})$ is a rotation of the second qubit around the axis $\mathbf{n} = (\sin \theta \cos \phi, \sin \theta \sin \phi, \cos \theta)$. U_{MPS} is simply an arbitrary controlled rotation on the second qubit conditional on the first being $|0\rangle$, combined with a SWAP gate. The unitary is made up of two CNOT

gates and one SWAP gate which are Clifford gates, and two local rotations which are non-Clifford and responsible for the non-stabilizerness of the MPS wave function.

The subtlety, however, is that the non-Clifford unitaries are only relevant if they act non-trivially on the input state. The first qubit always acts upon $|0\rangle$ by construction, and in the thermodynamic limit the second qubit acts on ρ_R , the right eigenvalue of the MPS transfer matrix $E = \sum_{\sigma} A^{\sigma} \otimes \bar{A}^{\sigma}$. It is thus natural to expect that the non-stabilizerness of the MPS is given by the non-stabilizerness of $\rho_{\text{in}} = |0\rangle\langle 0| \otimes \rho_R$ with U_{MPS} applied to it, minus the non-stabilizerness of ρ_{in} ,

$$m_U^{(2)} = m^{(2)}(U_{\text{MPS}}\rho_{\text{in}}U_{\text{MPS}}^{\dagger}) - m^{(2)}(\rho_R), \quad (6)$$

where we have taken advantage of the SRE additivity under tensor product to write $m^{(2)}(\rho_{\text{in}}) = m^{(2)}(\rho_R)$. Due to the inherent gauge freedom in our MPS, U_{MPS} is only unique up to a unitary transformation, $U_{\text{MPS}} \rightarrow (u \otimes \mathbb{1}_d)U_{\text{MPS}}(u \otimes \mathbb{1}_d)$, where u is an arbitrary $\chi \times \chi$ unitary matrix. Since u can be non-Clifford, it can change $m_U^{(2)}$. The gauge chosen throughout this paper is the only natural choice for the PXP model: the form of ρ_{in} and U_{MPS} guarantees that the $|11\rangle$ component of the MPS remains zero, ensuring that the Rydberg blockade constraint is also obeyed by the unitary generating the MPS.

In Fig. 1(f) we compare the non-stabilizerness obtained from the MPS ansatz in Fig. 1(b) against $m_U^{(2)}$ in Eq. (6). We observe an excellent agreement between the two over the range in which we traverse diagonally through one of the arrow shaped regions, especially at the two extremes of the θ range. In the region of high non-stabilizerness, our ansatz in Eq. (6) slightly deviates from the exact $m^{(2)}$, implying that U_{MPS} is not the exact unitary and further corrections may be needed to exactly capture the SRE across the entire manifold \mathcal{M} . In the SM [48], we present another example where analogous $m_U^{(2)}$ exactly describes the SRE of a cluster-Ising ground state.

Experimental protocol.—Finally, we outline two experimental protocols for accessing the non-stabilizer states in Fig. 1. We consider a one-dimensional array of Rydberg atoms [39]

$$H_{\text{Ryd}} = \Omega \sum_j \sigma_j^y + \Delta \sum_j n_j + V \sum_{i < j} \frac{n_i n_j}{|i - j|^{\alpha}}, \quad (7)$$

with $n_j = |1\rangle\langle 1|_j$ counts local excitations, Δ is the chemical potential, and V is the overall strength of the van der Waals interactions. Due to the fast decay of the interactions ($\alpha=6$), we neglect interaction terms beyond next-nearest neighbors.

The Hamiltonian H_{Ryd} reduces to the PXP model in the regime $V \gg \Omega, \Delta$ [40, 49, 50]. In this regime, the non-stabilizerness in Fig. 1 can be accessed by repeating the same type of quench experiments performed in Ref. [39]. While measuring the global SRE may not be feasible,

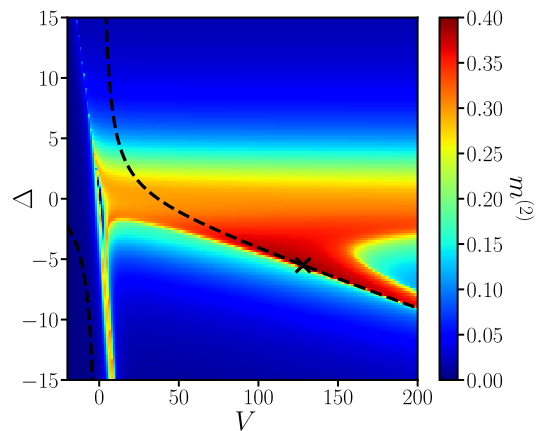


Figure 2. Phase diagram of the SRE for the ground state of the Rydberg model in Eq. (7) with $N=51$ atoms. We set $\Omega=1$ and vary Δ and V . Due to the large van der Waals decay exponent $\alpha=6$, we truncate the interactions to next-nearest neighbors. The ground state was obtained using DMRG based on ITensor Library [60] at a bond dimension of $\chi=4$. The dashed black line represents the path of the effective model (8) through the phase diagram, with the cross marking the point of maximal non-stabilizerness ($z \approx 2$) observed in Fig. 1.

the SRE can be approximated locally using a two-site reduced density matrix [48]. Note that, in order to be consistent with Fig. 1(c) where $\langle \sum_j \sigma_j^x \rangle = 0$, we have oriented the Rabi flip term in Eq. (7) along the y -axis, however this does not affect the value of the SRE.

Alternatively, it is possible to access the non-stabilizerness in Fig. 1 by adiabatic ground state preparation. With the reparametrization $\Delta = -\Omega(3z - 1/z)$ and $V = 2^\alpha \Omega z$, the ground state of H_{Ryd} for $z \gtrsim 1$ can be approximated with the ground state of the following frustration-free Hamiltonian [61, 62]:

$$H_0 = \sum_{j=1}^N P_{j-1} (\sigma_j^y + z P_j + z^{-1} n_j) P_{j+1}. \quad (8)$$

The ground state of H_0 is known exactly for any value of z [61]. In the SM [48], we prove that the ground state of H_0 is, in fact, equivalent to the MPS state in Eq. (4) with $\theta = \theta_o = \theta_e$ and $z = \sin(\theta/2) / \cos^2(\theta/2)$. Thus, the large non-stabilizerness in Fig. 1 can be generated by simply preparing the ground state of H_0 with $z \approx 2$.

In Fig. 2 we show the SRE phase diagram for the ground state of the Rydberg model for $N=51$ atoms and bond dimension $\chi=4$. Black line in Fig. 2 shows the path of H_0 in the full Rydberg model traced by varying z , with the cross marking the peak in the SRE. We see a band of large non-stabilizerness which becomes more pronounced with stronger blockade V . H_0 passes through the region of maximal non-stabilizerness attaining the maximum value of $m^{(2)} \approx 0.38$, which is close to the value of $m^{(2)} \approx 0.42$ found for the MPS ansatz.

Conclusions and outlook.—We have shown that kinetic constraints stemming from the Rydberg blockade can lead to many-body non-stabilizerness. Our study focused on the tractable example of the PXP model, where recently developed MPS framework for scarred dynamics allowed us to demonstrate how non-stabilizerness emerges microscopically using a quantum circuit construction. In particular, we argued that non-equilibrium dynamics is a useful mechanism for generating these non-stabilizer states in experiment. Further results about the non-stabilizerness of eigenstates in the PXP model can be found in the SM [48].

The exploration of non-stabilizerness in MPS states from a quantum circuit perspective deserves further study. While our approach can be applied to other models [48], the MPS has an intrinsic ambiguity due to the gauge degree of freedom, which should be better understood at the general level. Furthermore, our work highlights the fact that some low bond-dimension MPS can exhibit high levels of non-stabilizerness. Since all area-law entangled states in one dimension can be approximated by MPS, this implies that ground states of many physical systems may be difficult to create in an error correcting quantum computer. Finally, an interesting open question regarding non-stabilizerness in many-body systems is which wave functions saturate its upper bound. Rydberg atom arrays exhibit a variety of exotic phases [63, 64] and it would be interesting to study the non-stabilizerness in their ground states to see if one can further approach the upper bound.

Acknowledgments.—We would like to thank Abolfazl Bayat, Benjamin Béri, Jad Halimeh, David Jennings, and Jie Ren for inspiring discussions. We acknowledge support by the Leverhulme Trust Research Leadership Award RL-2019-015 and the EPSRC International Quantum Tensor Network EP/W026848/1. Statement of compliance with EPSRC policy framework on research data: This publication is theoretical work that does not require supporting research data. This work made use of the High Performance Computing facilities at the University of Leeds, UK. ZP acknowledges support by grants NSF PHY-1748958 and PHY-2309135 to the Kavli Institute for Theoretical Physics (KITP).

-
- [1] A. Kitaev and J. Preskill, *Phys. Rev. Lett.* **96**, 110404 (2006).
 [2] M. Levin and X.-G. Wen, *Phys. Rev. Lett.* **96**, 110405 (2006).
 [3] H. Li and F. D. M. Haldane, *Phys. Rev. Lett.* **101**, 010504 (2008).
 [4] F. Pollmann, E. Berg, A. M. Turner, and M. Oshikawa, *Phys. Rev. B* **85**, 075125 (2012).
 [5] P. Calabrese and J. Cardy, *Journal of Statistical Mechanics: Theory and Experiment* **2005**, P04010 (2005).
 [6] J. H. Bardarson, F. Pollmann, and J. E. Moore, *Phys. Rev. Lett.* **109**, 017202 (2012).
 [7] M. Serbyn, Z. Papić, and D. A. Abanin, *Phys. Rev. Lett.* **110**, 260601 (2013).
 [8] A. Lukin, M. Rispoli, R. Schittko, M. E. Tai, A. M. Kaufman, S. Choi, V. Khemani, J. Léonard, and M. Greiner, *Science* **364**, 256–260 (2019).
 [9] N. Laflorencie, *Physics Reports* **646**, 1 (2016).
 [10] U. Schollwöck, *Annals of Physics* **326**, 96 (2011), january 2011 Special Issue.
 [11] J. I. Cirac, D. Pérez-García, N. Schuch, and F. Verstraete, *Rev. Mod. Phys.* **93**, 045003 (2021).
 [12] S. R. White, *Phys. Rev. Lett.* **69**, 2863 (1992).
 [13] D. Gottesman, The heisenberg representation of quantum computers (1998), [arXiv:quant-ph/9807006](https://arxiv.org/abs/quant-ph/9807006) [quant-ph].
 [14] B. Eastin and E. Knill, *Phys. Rev. Lett.* **102**, 110502 (2009).
 [15] E. Knill, Fault-tolerant postselected quantum computation: Schemes (2004), [arXiv:quant-ph/0402171](https://arxiv.org/abs/quant-ph/0402171) [quant-ph].
 [16] S. Bravyi and A. Kitaev, *Phys. Rev. A* **71**, 022316 (2005).
 [17] E. T. Campbell and D. E. Browne, *Phys. Rev. Lett.* **104**, 030503 (2010).
 [18] M. Howard and E. Campbell, *Phys. Rev. Lett.* **118**, 090501 (2017).
 [19] S. Zhou, Z.-C. Yang, A. Hamma, and C. Chamon, *SciPost Phys.* **9**, 087 (2020).
 [20] K. Goto, T. Nosaka, and M. Nozaki, Chaos by magic (2021), [arXiv:2112.14593](https://arxiv.org/abs/2112.14593).
 [21] Z.-W. Liu and A. Winter, *PRX Quantum* **3**, 020333 (2022).
 [22] L. Leone, S. F. E. Oliviero, and A. Hamma, *Phys. Rev. Lett.* **128**, 050402 (2022).
 [23] T. Haug and L. Piroli, *Phys. Rev. B* **107**, 035148 (2023).
 [24] P. S. Tarabunga, E. Tirrito, T. Chanda, and M. Dalmonte, *PRX Quantum* **4**, 040317 (2023).
 [25] X. Turkeshi, M. Schirò, and P. Sierant, *Phys. Rev. A* **108**, 042408 (2023).
 [26] M. Bejan, C. McLauchlan, and B. Béri, Dynamical magic transitions in monitored clifford+t circuits (2023), [arXiv:2312.00132](https://arxiv.org/abs/2312.00132).
 [27] P. Niroula, C. D. White, Q. Wang, S. Johri, D. Zhu, C. Monroe, C. Noel, and M. J. Gullans, Phase transition in magic with random quantum circuits (2024), [arXiv:2304.10481](https://arxiv.org/abs/2304.10481).
 [28] P. S. Tarabunga and C. Castelnovo, *Quantum* **8**, 1347 (2024).
 [29] T. Haug, L. Aolita, and M. S. Kim, Probing quantum complexity via universal saturation of stabilizer entropies (2024), [arXiv:2406.04190](https://arxiv.org/abs/2406.04190).
 [30] S. F. E. Oliviero, L. Leone, A. Hamma, and S. Lloyd, *npj Quantum Information* **8**, 148 (2022).
 [31] M. Heinrich and D. Gross, *Quantum* **3**, 132 (2019).
 [32] S. Sarkar, C. Mukhopadhyay, and A. Bayat, *New Journal of Physics* **22**, 083077 (2020).
 [33] P. S. Tarabunga, Critical behaviours of non-stabilizerness in quantum spin chains (2024), [arXiv:2309.00676](https://arxiv.org/abs/2309.00676) [quant-ph].
 [34] M. Frau, P. S. Tarabunga, M. Collura, M. Dalmonte, and E. Tirrito, Non-stabilizerness versus entanglement in matrix product states (2024), [arXiv:2404.18768](https://arxiv.org/abs/2404.18768) [quant-ph].
 [35] G. Lami and M. Collura, Quantum magic via per-

- fect pauli sampling of matrix product states (2023), [arXiv:2303.05536 \[quant-ph\]](#).
- [36] Z. Liu and B. K. Clark, Non-equilibrium quantum monte carlo algorithm for stabilizer rényi entropy in spin systems (2024), [arXiv:2405.19577 \[quant-ph\]](#).
- [37] T. Haug and L. Piroli, *Quantum* **7**, 1092 (2023).
- [38] P. S. Tarabunga, E. Tirrito, M. C. Bañuls, and M. Dalmonte, Nonstabilizerness via matrix product states in the pauli basis (2024), [arXiv:2401.16498 \[quant-ph\]](#).
- [39] H. Bernien, S. Schwartz, A. Keesling, H. Levine, A. Omran, H. Pichler, S. Choi, A. S. Zibrov, M. Endres, M. Greiner, V. Vuletić, and M. D. Lukin, *Nature* **551**, 579 (2017).
- [40] C. J. Turner, A. A. Michailidis, D. A. Abanin, M. Serbyn, and Z. Papić, *Nature Physics* **14**, 745 (2018).
- [41] C. J. Turner, A. A. Michailidis, D. A. Abanin, M. Serbyn, and Z. Papić, *Phys. Rev. B* **98**, 155134 (2018).
- [42] M. Serbyn, D. A. Abanin, and Z. Papić, *Nature Physics* **17**, 675 (2021).
- [43] Z. Papić, in *Entanglement in Spin Chains: From Theory to Quantum Technology Applications* (Springer, 2022) pp. 341–395.
- [44] S. Moudgalya, B. A. Bernevig, and N. Regnault, *Reports on Progress in Physics* **85**, 086501 (2022).
- [45] A. Chandran, T. Iadecola, V. Khemani, and R. Moessner, *Annual Review of Condensed Matter Physics* **14**, 443 (2023).
- [46] W. W. Ho, S. Choi, H. Pichler, and M. D. Lukin, *Phys. Rev. Lett.* **122**, 040603 (2019).
- [47] A. A. Michailidis, C. J. Turner, Z. Papić, D. A. Abanin, and M. Serbyn, *Phys. Rev. X* **10**, 011055 (2020).
- [48] See the Supplemental Material for detailed information about the calculations and results in the main text.
- [49] P. Fendley, K. Sengupta, and S. Sachdev, *Phys. Rev. B* **69**, 075106 (2004).
- [50] I. Lesanovsky and H. Katsura, *Phys. Rev. A* **86**, 041601 (2012).
- [51] A. Browaeys and T. Lahaye, *Nature Physics* **16**, 132 (2020).
- [52] C.-J. Lin and O. I. Motrunich, *Phys. Rev. Lett.* **122**, 173401 (2019).
- [53] T. Iadecola, M. Schechter, and S. Xu, *Phys. Rev. B* **100**, 184312 (2019).
- [54] V. Khemani, C. R. Laumann, and A. Chandran, *Phys. Rev. B* **99**, 161101 (2019).
- [55] S. Choi, C. J. Turner, H. Pichler, W. W. Ho, A. A. Michailidis, Z. Papić, M. Serbyn, M. D. Lukin, and D. A. Abanin, *Phys. Rev. Lett.* **122**, 220603 (2019).
- [56] K. Bull, J.-Y. Desaules, and Z. Papić, *Phys. Rev. B* **101**, 165139 (2020).
- [57] K. Omiya and M. Müller, *Phys. Rev. A* **107**, 023318 (2023).
- [58] J. Haegeman, J. I. Cirac, T. J. Osborne, I. Pizorn, H. Verschelde, and F. Verstraete, *Phys. Rev. Lett.* **107**, 070601 (2011).
- [59] G. Vidal, *Phys. Rev. Lett.* **91**, 147902 (2003).
- [60] M. Fishman, S. R. White, and E. M. Stoudenmire, *SciPost Phys. Codebases*, 4 (2022).
- [61] I. Lesanovsky, *Phys. Rev. Lett.* **106**, 025301 (2011).
- [62] I. Lesanovsky, *Phys. Rev. Lett.* **108**, 105301 (2012).
- [63] A. Keesling, A. Omran, H. Levine, H. Bernien, H. Pichler, S. Choi, R. Samajdar, S. Schwartz, P. Silvi, S. Sachdev, P. Zoller, M. Endres, M. Greiner, V. Vuletić, and M. D. Lukin, *Nature* **568**, 207 (2019).
- [64] G. Semeghini, H. Levine, A. Keesling, S. Ebadi, T. T. Wang, D. Bluvstein, R. Verresen, H. Pichler, M. Kalinowski, R. Samajdar, A. Omran, S. Sachdev, A. Vishwanath, M. Greiner, V. Vuletić, and M. D. Lukin, *Science* **374**, 1242 (2021).
- [65] N. G. Jones, J. Bibo, B. Jobst, F. Pollmann, A. Smith, and R. Verresen, *Phys. Rev. Res.* **3**, 033265 (2021).
- [66] M. M. Wolf, G. Ortiz, F. Verstraete, and J. I. Cirac, *Phys. Rev. Lett.* **97**, 110403 (2006).
- [67] A. Smith, B. Jobst, A. G. Green, and F. Pollmann, *Phys. Rev. Res.* **4**, L022020 (2022).
- [68] P. Kramer and M. Saraceno, *Geometry of the Time-Dependent Variational Principle in Quantum Mechanics*, Lecture Notes in Physics (Springer Berlin Heidelberg, 1981).
- [69] M. Ahmadi, H. B. Dang, G. Gour, and B. C. Sanders, *Phys. Rev. A* **97**, 062332 (2018).
- [70] A. N. Ivanov and O. I. Motrunich, Volume-entangled exact eigenstates in the pxp and related models in any dimension (2024), [arXiv:2403.05515 \[quant-ph\]](#).

Supplemental Online Material for “Non-stabilizerness in kinetically-constrained Rydberg atom arrays”

In this Supplemental Material, we provide details of our calculations of Stabilizer Renyi Entropies (SREs) for finite and infinite matrix product states (MPS). In addition to the PXP model, we illustrate our approach on the MPS skeleton model [65], where the behavior of SRE can be transparently understood in the unitary circuit formalism. We discuss the effect of local unitary rotations on the SRE. We compute the non-stabilizerness of eigenstates in the PXP model using exact diagonalization and Monte Carlo sampling, as well as via replica MPS method for special PXP eigenstates that have an exact $\chi=2$ MPS representation.

CALCULATING STABILIZER RENEYI ENTROPIES FOR MATRIX PRODUCT STATES

In this section we review the method for calculating the SRE of a state expressed as an MPS. We will briefly describe the method for both finite systems and infinite systems described by an N -site translation-invariant unit cell. This section does not contain any new results and reviews the method introduced in Ref. [23].

Firstly, we consider a normalized state $|\psi\rangle$ of a N -particle spin- $\frac{1}{2}$ chain which is represented by an MPS of physical dimension d and bond dimension χ . We denote by $\{\sigma^\alpha\} = \{\mathbb{1}, \sigma^x, \sigma^y, \sigma^z\}$ the four Pauli operators and define \mathcal{P}_N as the set of all N -qubit Pauli strings. To calculate the n th order SRE, we begin by creating a $2n$ -fold replica of the state $|\phi^{(n)}\rangle = |\psi\rangle^{\otimes 2n}$ with physical dimension $d' = d^{2n}$ and bond dimension $\chi' = \chi^{2n}$. Since we are only considering the $n = 2$ SRE we introduce $\Lambda_j^{(n)} = \frac{1}{2} \sum^3 (\sigma_j^\alpha)^{\otimes 2n}$ which acts over every $2n$ replica of $|\psi\rangle$ on a physical site j . Therefore, the expectation value of all the N -qubit Pauli strings can be seen as the single expectation value:

$$\sum_{P \in \mathcal{P}_N} \frac{\langle \psi | P | \psi \rangle^{2n}}{2^N} = \langle \phi^{(n)} | \Lambda_1^{(n)} \otimes \dots \otimes \Lambda_N^{(n)} | \phi^{(n)} \rangle, \quad (\text{S1})$$

which we will denote as $\langle \phi^{(n)} | \Lambda^{(n)} | \phi^{(n)} \rangle$. Thus, the many-body SRE is:

$$M^{(n)}(|\psi\rangle) = (1 - n)^{-1} \ln \langle \phi^{(n)} | \Lambda^{(n)} | \phi^{(n)} \rangle, \quad (\text{S2})$$

and the SRE density can be defined as $m^{(n)} = M^{(n)}/N$. In the main text, we always make use of the SRE density $m^{(n)}$, as an intensive quantity that can also be defined for a state on an infinite lattice, discussed next.

Similarly, we can consider a normalized state on an infinite chain of spins which can be described by an N -site translation-invariant unit cell defined by N three-legged MPS tensor A_{ij}^σ with bond dimension χ and physical dimension d . We create a $2n$ -fold replica of A_{ij}^σ defined as $B_{ij}^{\sigma^s} = (A_{ij}^\sigma)^{\otimes 2n}$ with bond dimension $\chi' = \chi^{2n}$ and physical dimension $d' = d^{2n}$. Working in the thermodynamic limit, we introduce the $\chi^{4n} \times \chi^{4n}$ transfer matrix

$$\tau_{(ik),(jl)} = \sum_{s,s'} B_{i,j}^{\sigma^s} (\Lambda_1^{(n)} \otimes \dots \otimes \Lambda_N^{(n)})_{\sigma_s, \sigma_{s'}} \bar{B}_{k,l}^{\sigma^{s'}}, \quad (\text{S3})$$

which will have a dominant eigenvalue $\lambda_0^{(n)}$ (in absolute terms) and the SRE is

$$m^{(n)}(|\psi(A)\rangle) = (1 - n)^{-1} \ln \lambda_0^{(n)}. \quad (\text{S4})$$

Below we illustrate this computation on a concrete physical example where $m^{(2)}$ can be obtained in closed form.

NON-STABILIZERNESS OF A MATRIX PRODUCT STATE SKELETON

In addition to the PXP model considered in the main text, our approach can also be applied to a variant of the cluster Ising model that possesses a so-called MPS skeleton ground state [65–67]. The model is defined by the following spin-1/2 chain Hamiltonian

$$H = g_{zxx} \sum_i \sigma_i^z \sigma_{i+1}^x \sigma_{i+2}^z - g_{zz} \sum_i \sigma_i^z \sigma_{i+1}^z - g_x \sum_i \sigma_i^x, \quad (\text{S5})$$

where the first three-body term is the cluster term that is added to the Ising model in a transverse field (the last two terms). This Hamiltonian is symmetric under time reversal and also under global spin flips generated by $\prod_i \sigma_i^x$. The phase diagram contains three distinct phases: a symmetry broken Ising phase, a trivial phase with a product ground state, and a symmetry protected topological phase (SPT). These three phases meet at a tricritical point.

There is a path through the phase diagram of the model in Eq. (S5) which traverses through the SPT and trivial phases, while also passing through the tricritical point. This path can be conveniently parameterized with a single variable g [66] according to:

$$H = \sum_i (g-1)^2 \sigma_i^z \sigma_{i+1}^x \sigma_{i+2}^z + 2(g^2-1) \sigma_i^z \sigma_{i+1}^z - (1+g)^2 \sigma_i^x, \quad (\text{S6})$$

with $g = -1$ corresponding to the pure cluster Hamiltonian and $g = 1$ corresponding to the paramagnet, with the tricritical point at $g = 0$ [66]. Along this entire path, the ground state is exactly described by the following $\chi = 2$ bond dimension MPS:

$$M^0 = \frac{1}{\sqrt{1+|g|}} \begin{pmatrix} 0 & 0 \\ \sqrt{|g|} & 1 \end{pmatrix}, \quad M^1 = \frac{1}{\sqrt{1+|g|}} \begin{pmatrix} 1 & \text{sign}(g)\sqrt{|g|} \\ 0 & 0 \end{pmatrix}. \quad (\text{S7})$$

This state was dubbed the MPS skeleton [65]. It is curious that the MPS skeleton describes exactly the ground state even at the critical point $g = 0$, despite the fact that the entanglement entropy there is strictly bounded by $\ln 2$. This is because the critical point is tricritical and there is no divergence of entanglement entropy with subsystem size, unlike in second-order Ising transitions which are also present in the same model in Eq. (S5).

Since the ground state along the g -trajectory is a $\chi = 2$ MPS, it is straightforward to calculate the SRE of the MPS ansatz (S7) using the replica method described above, yielding

$$m^{(2)}(g) = -\ln \left(\frac{1 + 14g^2 + g^4}{(1+|g|)^4} \right). \quad (\text{S8})$$

We plot this in Fig. S1(b), while Fig. S1(a) shows the SRE across the full g_x - g_{zz} - g_{zxz} phase diagram. The latter is obtained numerically using DMRG with fixed bond dimension $\chi = 4$.

There are several noteworthy aspects of Fig. S1. For $g = -1, 0, 1$ the SRE vanishes, $m^{(2)} = 0$, implying the ground state at these points is a stabilizer state. For $g = -1$, we are deep in the SPT phase and the ground state of the skeleton is the cluster state, which we know can be represented as a graph state and hence a stabilizer state. For $g = +1$, we are deep in the trivial phase, hence its product ground state is also a stabilizer state. Finally, for $g = 0$ we are located at the tricritical point where the ground state is a Greenberger-Horne-Zeilinger (GHZ) state, which is also a stabilizer state since it can be prepared using only Clifford gates. The more surprising feature is the peak of non-stabilizerness which can be seen in Fig. S1(b). From Eq. (S8), it is easy to show that the peak occurs at $g = \pm(3 - 2\sqrt{2})$, with the peak value of $m^{(2)} \approx 0.28$, which is comparable to the SRE of the Ising model at its critical point [24, 36].

To explain the SRE peaks for the MPS skeleton in Fig. S1(b), we follow the same approach as in the main text and consider the unitary which generates the MPS ground state. We can interpret our MPS description of the ground state to be a unitary acting on the reference state $|0\rangle$. It was shown in Ref. [67] that this MPS can be embedded into a 2-qubit unitary with one site acting on $|0\rangle$ and decomposed into the quantum circuit:



where the unitaries U_V and U_W are defined by the angles $\theta_v = \arcsin(\sqrt{|g|}/\sqrt{1+|g|})$ and $\theta_w = \arccos(\text{sign}(g)\sqrt{|g|}/\sqrt{1+|g|})$ and matrix elements

$$U = \begin{pmatrix} \sin \theta & \cos \theta \\ \cos \theta & -\sin \theta \end{pmatrix}. \quad (\text{S10})$$

The quantum circuit above only has two non-Clifford gates, therefore the circuit unitary will have maximum non-stabilizerness if and only if unitaries V and W are maximally non-Clifford. This occurs when $\theta_v = \pm\pi/8$ and $\theta_w = \pm 3\pi/8$ which are precisely the same points as $g = \pm(3 - 2\sqrt{2})$, thus explaining the location of the peaks in the SRE. In fact, the unitary magic $m_U^{(2)}$ is exactly equal to Eq. (S8) for all g provided the gauge used in Eq. (S7) is used.

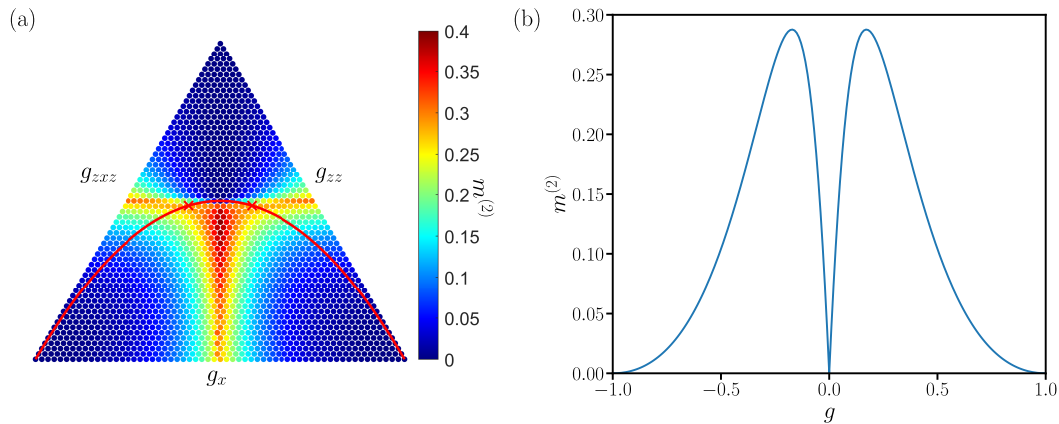


Figure S1. (a) The SRE $m^{(2)}$ across the phase diagram of the cluster Ising model in Eq. (S5). The SRE is computed numerically using DMRG with bond dimension $\chi = 6$. Red line marks the trajectory of the skeleton model in Eq. (S6), with the cross corresponding to the maximal non-stabilizerness. (b) The SRE for the MPS ground state of Eq. (S6) as it interpolates between the SPT phase and the trivial phase. The peaks in $m^{(2)}$ are located at $g = \pm(3 - 2\sqrt{2})$, which correspond to the points where the unitary which describes the embedding of the MPS ansatz are maximally non-Clifford.

MATRIX PRODUCT STATE ANSATZ FOR PXP DYNAMICS AND ITS PARENT HAMILTONIAN

In this section we provide a brief overview of the MPS manifold and the equations of motion (EOMs) used in the main text. The complete derivation and generalizations to PXP models with higher spin magnitude $s > 1/2$ can be found in Ref. [46], which we follow here. At the end of this section, we derive the parent Hamiltonian for the studied MPS, showing that, under certain conditions, it is equivalent to the model introduced in Ref. [61]. To the best of our knowledge, this connection has not been made in the previous literature.

Time dependent variational principle for MPS manifold in the PXP model

Time-dependent variational principle (TDVP) is a widely used technique for approximating the dynamics of a quantum system in a suitable manifold of states [68]. We consider the geometric principle formulation, which ensures the dynamics always remain in the manifold due to the time evolved state being continuously projected into the manifold's tangent space. For a manifold parameterized by variables \mathbf{z} , we minimize the vector orthogonal to the tangent space,

$$\min_{\mathbf{z}} \|\dot{\mathbf{z}} \partial_{\mathbf{z}} |\psi(\mathbf{z})\rangle + iH |\psi(\mathbf{z})\rangle\|, \quad (\text{S11})$$

which leads to the equations of motion

$$\sum_k \langle \partial_{z_l} \psi(\mathbf{z}) | \partial_{z_k} \psi(\mathbf{z}) \rangle \dot{z}_k + i \langle \partial_{z_l} \psi(\mathbf{z}) | H | \psi(\mathbf{z}) \rangle = 0, \quad (\text{S12})$$

where $\langle \partial_{z_l} \psi(\mathbf{z}) | \partial_{z_k} \psi(\mathbf{z}) \rangle$ is the Gram matrix.

The above expressions are valid for any kind of manifold with a continuous parametrization. In our case, the manifold is spanned by MPS states [58]. Firstly, the $s = 1/2$ spin coherent state on a single site is defined as $|\psi(\theta, \phi)\rangle = \cos(\theta/2) |0\rangle - e^{i\phi} \sin(\theta/2) |1\rangle$. In the Rydberg blockaded basis, the corresponding MPS can be written as:

$$A^0(\theta, \phi) = \begin{pmatrix} \cos(\theta/2) & 0 \\ 1 & 0 \end{pmatrix}, \quad A^1(\theta, \phi) = \begin{pmatrix} 0 & -e^{i\phi} \sin(\theta/2) \\ 0 & 0 \end{pmatrix}. \quad (\text{S13})$$

This MPS is equivalent to the one used in the main text up to a gauge transformation. The current gauge choice is convenient for calculating the TDVP equations of motion for MPS angles $\mathbf{z} \equiv (\theta, \phi)$ which parametrize our manifold.

The one-site transfer matrix is given by

$$T(\theta, \phi) = A(\theta, \phi)^\dagger \otimes A(\theta, \phi) = \begin{pmatrix} \cos^2(\theta/2) & 0 & 0 & \sin^2(\theta/2) \\ \cos(\theta/2) & 0 & 0 & 0 \\ \cos(\theta/2) & 0 & 0 & 0 \\ 1 & 0 & 0 & 0 \end{pmatrix}. \quad (\text{S14})$$

Since we are only interested in the dynamics of the states $|0\rangle$ and $|\mathbb{Z}_2\rangle$ we instead require a translationally invariant two-site unit cell defined with parameters $(\theta_{2i}, \phi_{2i}) = (\theta_e, \phi_e)$ and $(\theta_{2i+1}, \phi_{2i+1}) = (\theta_o, \phi_o)$ with transfer matrix $T(\theta_o, \phi_o, \theta_e, \phi_e) = T(\theta_o, \phi_o)T(\theta_e, \phi_e)$. This matrix has 4 eigenvalues λ_i and 4 left $\langle l_i|$ and right $|r_i\rangle$ eigenvectors, which can be found in Ref. [46].

Choosing $|0\rangle$ and $|\mathbb{Z}_2\rangle$ as initial states allows us to make an important simplification and set $\phi_e = \phi_o = 0$. We will show that this follows because $(\dot{\phi}_e, \dot{\phi}_o) = (0, 0)$. We consider the energy expectation value $\langle \psi(\theta, \phi) | H | \psi(\theta, \phi) \rangle$ for the PXP Hamiltonian $H = (\Omega/2) \sum_i P_{i-1} \sigma_i^x P_{i+1}$. We define:

$$h(\theta, \phi) = A(\theta, \phi)^\dagger \otimes (\sigma^x A(\theta, \phi)) = \begin{pmatrix} 0 & a^*b & ab^* & c - a^*b - ab^* \\ 0 & 0 & b^* & 0 \\ 0 & b & 0 & 0 \\ 0 & 0 & 0 & 0 \end{pmatrix}, \quad (\text{S15})$$

where $a = \cos(\theta/2)$, $b = i \sin(\theta/2) e^{i\phi}$ and $c = (\sin \theta \sin \phi)/2$. Now the energy expectation value can be evaluated as:

$$\begin{aligned} \langle \psi(\theta, \phi) | H | \psi(\theta, \phi) \rangle &= \frac{N\Omega}{2} \sum_{i=1}^4 \langle l_i | h(\theta_o, \phi_o) T(\theta_e, \phi_e) + T(\theta_o, \phi_o) h(\theta_e, \phi_e) | r_i \rangle \\ &= \frac{N\Omega}{2} \frac{\cos(\theta_o/2) \cos^3(\theta_e/2) \sin(\theta_o/2) \sin(\phi_o)}{\cos^2(\theta_o/2) + \cos^2(\theta_e/2) - \cos^2(\theta_o/2) \cos^2(\theta_e/2)} + (e \leftrightarrow o). \end{aligned} \quad (\text{S16})$$

We can see that if $(\phi_o, \phi_e) = (0, 0)$, then $\langle \psi(\theta, \phi) | H | \psi(\theta, \phi) \rangle = 0$, which implies that the energies of the states $|0\rangle$ and $|\mathbb{Z}_2\rangle$ is also zero. Since the TDVP equations of motion are energy-conserving, we can set $(\dot{\phi}_e, \dot{\phi}_o) = (0, 0)$ and drop all dependence on $\phi_{e,o}$ during the time evolution and also when computing the SRE across the manifold.

Now we will turn our attention to determining the equations of motion for $A(\theta)$. We need two things, the Gram matrix and the dynamical term. Both of these were calculated in Ref. [46]. For the Gram matrix, the two off-diagonal terms conveniently vanish, $G_{oe}, G_{eo} = 0$, leading to only two equations of motion:

$$\begin{aligned} \dot{\theta}_o &= G_{oo}^{-1} i \langle \partial_{\theta_o} \psi(\theta_o, \theta_e) | H | \psi(\theta_o, \theta_e) \rangle, \\ \dot{\theta}_e &= G_{ee}^{-1} i \langle \partial_{\theta_e} \psi(\theta_o, \theta_e) | H | \psi(\theta_o, \theta_e) \rangle. \end{aligned} \quad (\text{S17})$$

For spin-1/2 case, these are shown to be:

$$\begin{aligned} \dot{\theta}_o &= \cos\left(\frac{\theta_e}{2}\right) + \sin\left(\frac{\theta_o}{2}\right) \tan\left(\frac{\theta_e}{2}\right) \cos^2\left(\frac{\theta_o}{2}\right), \\ \dot{\theta}_e &= \cos\left(\frac{\theta_o}{2}\right) + \sin\left(\frac{\theta_e}{2}\right) \tan\left(\frac{\theta_o}{2}\right) \cos^2\left(\frac{\theta_e}{2}\right). \end{aligned} \quad (\text{S18})$$

Integrating this system of equations allows us to track the dynamics within the manifold in the main text.

Parent Hamiltonian for MPS ansatz

Every matrix-product state $|\psi(A)\rangle$ is the ground state of a so-called parent Hamiltonian which is a local, frustration-free Hamiltonian constructed as the sum of projectors $H^{\text{parent}} = \sum_j \mathbb{P}_j$ where $\mathbb{P}_j^2 = \mathbb{P}_j$. The particular MPS is in the null-space of the projector \mathbb{P}_j and therefore has energy exactly $E = 0$ with respect to this parent Hamiltonian. We would like to find a parent Hamiltonian for the MPS used in the main text:

$$A^0(\theta, \phi) = \begin{pmatrix} c & 0 \\ s & 0 \end{pmatrix}, \quad A^1(\theta, \phi) = \begin{pmatrix} 0 & -ie^{i\phi} \\ 0 & 0 \end{pmatrix}, \quad (\text{S19})$$

where $c \equiv \cos(\theta/2)$ and $s \equiv \sin(\theta/2)$. In this section, we will work in the thermodynamic limit and assume a single-site unit cell, as we are interested in the dynamics of $|0\rangle$ state.

The projector which defines the parent Hamiltonian for the MPS in Eq. (S19) is found by constructing the reduced density ρ_n of $|\psi(A)\rangle$ over n sites. The value of n should be chosen such that ρ_n has at least one eigenvalue zero. This is typically the case when $d^n > \chi^2$. For the PXP model, the Hilbert space obeys the Rydberg blockade constraint which excludes certain states, hence ρ_n does not grow exactly like d^n . Nevertheless, $n = 3$ is suitable since ρ_n has 5 eigenvalues, which is larger than the $\chi^2 = 4$.

We choose the basis $\{|000\rangle, |001\rangle, |010\rangle, |100\rangle, |101\rangle\}$ for ρ_3 . Utilizing the fact that the leading left/right eigenvalues of the MPS transfer matrix are $|\mathbb{L}\rangle = (1, 0, 0, 1)$ and $|\mathbb{R}\rangle = \frac{1}{1+s^2}(1, cs, cs, s^2)$, ρ_3 can be shown to be:

$$\rho_3 = \frac{1}{1+s^2} \begin{pmatrix} c^4 & -ic^4se^{i\phi} & -ic^2se^{i\phi} & -ic^4se^{i\phi} & -c^4s^2e^{2i\phi} \\ ic^4se^{-i\phi} & c^2s^2 & c^2s^2 & c^4s^2 & -ic^2s^3e^{i\phi} \\ ic^2se^{-i\phi} & c^2s^2 & s^2 & c^2s^2 & -ic^2s^3e^{i\phi} \\ ic^4se^{-i\phi} & c^4s^2 & c^2s^2 & c^2s^2 & -ic^2s^3e^{i\phi} \\ -c^4s^2e^{2i\phi} & ic^2s^3e^{-i\phi} & ic^2s^3e^{-i\phi} & ic^2s^3e^{-i\phi} & s^4 \end{pmatrix}. \quad (\text{S20})$$

Thus, ρ_3 has a single eigenvalue zero with eigenvector:

$$|\phi\rangle = \frac{1}{\sqrt{1+s^2/c^4}} \begin{pmatrix} ie^{i\phi}s/c^2 \\ 0 \\ 1 \\ 0 \\ 0 \end{pmatrix}. \quad (\text{S21})$$

If we define $z = s/c^2$, then the parent Hamiltonian of the MPS ansatz is $\mathbb{P}_j = |\phi\rangle\langle\phi|$, where

$$\begin{aligned} \mathbb{P}_j &= \frac{1}{1+z^2} (z^2 |000\rangle\langle 000| + |010\rangle\langle 010| - iz e^{-i\phi} |000\rangle\langle 010| + iz e^{i\phi} |010\rangle\langle 000|)_{j-1,j,j+1} \\ &= \frac{z}{1+z^2} P_{j-1} (z P_j + z^{-1} n_j + \cos(\phi) \sigma_j^y + \sin(\phi) \sigma_j^x) P_{j+1}. \end{aligned} \quad (\text{S22})$$

When $\phi = 0$, this is the model introduced in Ref. [61] and discussed in the main text, up to an overall prefactor. Although considerably more tedious, it is possible to generalize this to the case of 2-site unit cell which would be needed for describing the dynamics of the $|\mathbb{Z}_2\rangle$ state. We have not pursued this, however, since the non-stabilizerness along the $|\mathbb{Z}_2\rangle$ orbit is smaller than for the $|0\rangle$ state.

LOCAL VS GLOBAL NON-STABILIZERNESS

In the main text we noted that since the SRE depends upon N -site products of Pauli matrices spread throughout the entire system, it is therefore a global property of the wave function. In contrast, typical physical observables are spread over few physical sites and therefore can be calculated using the reduced density matrix of the wave function. In this section, we will address the extent to which the non-stabilizerness of the MPS ansatz is stored in local or global degrees of freedom.

As we discussed in the main text, the SRE is a basis dependent quantity, varying even for uncorrelated product states. For this reason, it is common to consider ‘‘long-range’’ non-stabilizerness, which is the minimum of the non-stabilizerness after an arbitrary local rotation on every site of the system. For the case of the MPS ansatz used in the PXP model, the only relevant rotation for reducing the SRE is the x -axis which may differ on odd and even sites of the unit cell, $|\psi\rangle \rightarrow |\tilde{\psi}(\gamma_o, \gamma_e)\rangle = \bigotimes_i (e^{i\gamma_o\sigma_{2i-1}^y} \otimes e^{i\gamma_e\sigma_{2i}^y}) |\psi\rangle$. The long-range SRE is now

$$m_L^{(2)} = \min_{\{\gamma_o, \gamma_e\}} m^{(2)}(|\tilde{\psi}(\gamma_o, \gamma_e)\rangle). \quad (\text{S23})$$

In Fig. S2(a) the long-range SRE for the MPS ansatz trajectories of the $|0\rangle$ and $|\mathbb{Z}_2\rangle$ states are shown. For the $|0\rangle$ state, we see the long-range SRE is slightly smaller than the SRE but not significantly different, indicating that most of the SRE is long-range for this trajectory. For the $|\mathbb{Z}_2\rangle$ state, we see a significant difference. The distinctive three-peak behavior we see for the SRE disappears for the long-range SRE, with only a single, smaller peak. For this reason, we argue that the two smaller peaks of the SRE can be considered primarily local, similar to the non-stabilizerness

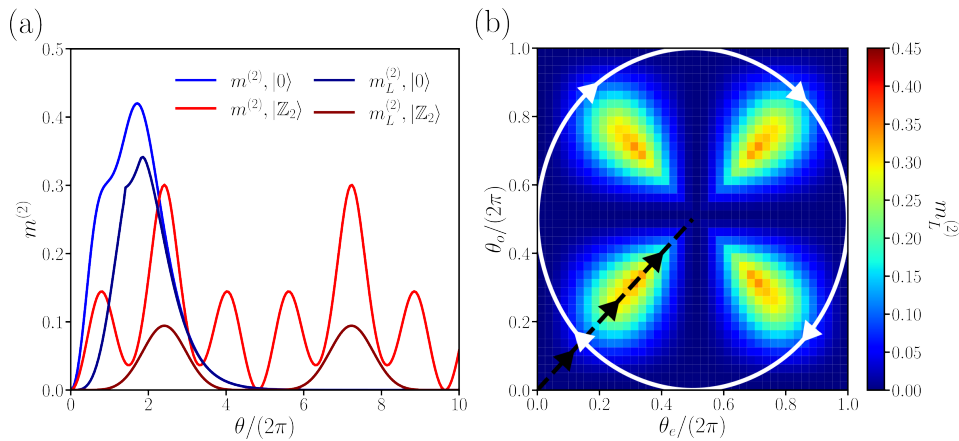


Figure S2. (a): Comparison of the TDVP dynamics between $m^{(2)}$ and the long range SRE $m_L^{(2)}$ for the $|0\rangle$ and the $|Z_2\rangle$ states showing the effects of local non-stabilizerness on the overall many-body SRE. (b): Phase diagram of the long range non-stabilizerness across the MPS manifold. The trajectories traversed by the $|Z_2\rangle$ and $|0\rangle$ states are shown by solid white and black dashed lines, respectively

of a product state. The central peak is a genuine many-body phenomenon, arising from correlated physics of the Rydberg blockade. Fig. S2(b) shows the long-range SRE across the entire MPS manifold. We see that the arrow-head structure identified in the main text vanishes for the long-range SRE, demonstrating that only the central areas of these arrow-heads are non-local.

Another approach to distinguishing local and global non-stabilizerness is to calculate the non-stabilizerness of a two-site reduced density matrix ρ_2 of the MPS ansatz's unit-cell. Since ρ_2 is a mixed state, the calculation of the SRE changes from the definition given in Eq. (1) to [22]:

$$M^{(2)}(\rho_2) = -\ln \left(\frac{\sum_{P \in \mathcal{P}_N} |\text{tr}(\rho_2 P)|^4}{\sum_{P \in \mathcal{P}_N} |\text{tr}(\rho_2 P)|^2} \right) \quad (\text{S24})$$

and the corresponding SRE density is $m^{(2)}(\rho_2) = M^{(2)}(\rho_2)/2$. For ease we will denote our two site reduced density matrix ρ_2 as ρ .

We also use a second measure for local non-stabilizerness called the ‘‘Robustness of Magic’’ (ROM) [18, 32, 69] which quantifies the minimal weight of stabilizer states that yields a stabilizer state when mixed with a density matrix ρ . Since the set of stabilizer states is overcomplete, it is possible to decompose ρ into a weighted sum of stabilizer states, $\rho = \sum_i X_i S_i$, where S_i is a stabilizer state, while satisfying the normalization constraint $\sum_i X_i = 1$. For ρ to have non-stabilizerness, at least one of the weights must be negative. Therefore the ROM is expressed as a convex optimization problem:

$$\mathcal{R} = \inf_{\{X_i\}} \left\{ \sum_i |X_i| - 1 : AX = B \right\}, \quad (\text{S25})$$

where $A_{\alpha\beta} = \text{tr}(\sigma^\alpha S_\beta)$ and $B_\alpha = \text{tr}(\sigma^\alpha \rho)$, with σ^α as a *two-qubit* Pauli string. However, the ROM is known to be multiplicative under tensor product therefore we instead define the ‘‘log free Robustness of Magic’’ $\log(\mathcal{R} + 1)$ [21] which is additive under tensor product and allows for a better comparison with SRE's. Since these two measures of non-stabilizerness rely only on the calculation of two-qubit expectation values, these measures provide an excellent ‘‘witness’’ for experimentally detecting non-stabilizerness.

In Fig. S3(a), the ROM for the two-site unit cell MPS is shown. While the ROM captures some of the arrowhead-like structure of the SRE, it diverges dramatically from the SRE in the long-range non-stabilizerness regions we identified in Fig. S2(b). Noticeably, a large area of stabilizerness is created at the centre of the unit cell where the points of the arrow-heads should be located. In Fig. S3(b) we see the SRE of the two-site reduced density matrix more accurately recreates the structures obtained in the full SRE calculation, although it also diverges in regions of large non-stabilizerness where the peak SRE is considerably lower, at around $m^{(2)}(\rho) \approx 0.32$ compared to a maximum of $m^{(2)} \approx 0.42$ for the full SRE. The ROM and 2-site SRE are consistent with the long-range non-stabilizerness, we see that the peak in the SRE is due to long-range non-stabilizerness that cannot be fully captured by local measurements. This underlines the importance of the unitary circuit construction discussed in the main text, where local quantities

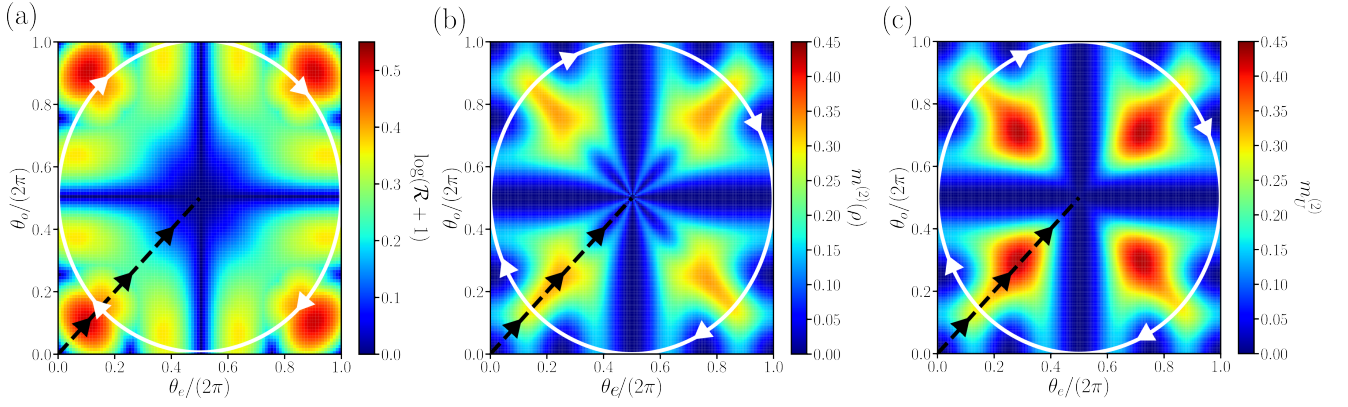


Figure S3. (a): Phase diagram for the “robustness of magic” \mathcal{R} across the MPS manifold \mathcal{M} . (b): Phase diagram for the SRE of the two site reduced density matrix of the MPS ansatz’s unit cell. (c): Phase diagram of the SRE obtained from the decomposition of the two site MPS being embedded into a two site unitary matrix. The trajectories traversed by the $|\mathbb{Z}_2\rangle$ and $|0\rangle$ states are shown by solid white and black dashed lines, respectively.

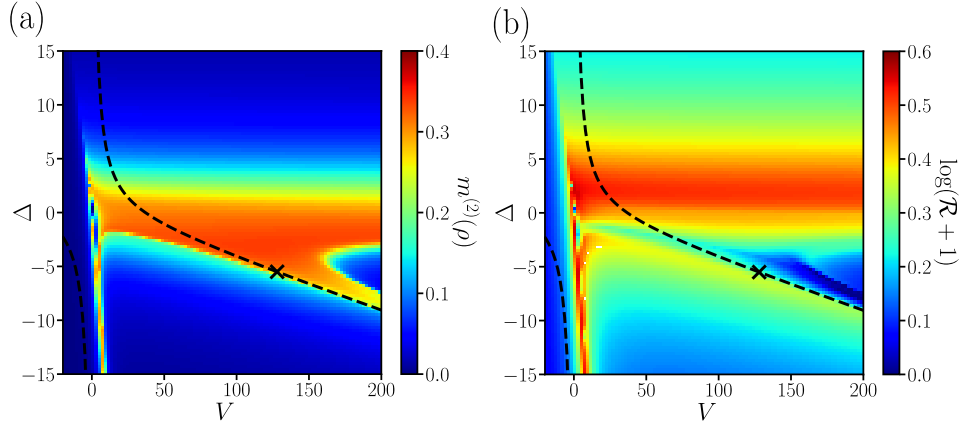


Figure S4. (a): Phase diagram of the two-site density matrix SRE $m^{(2)}$ for the ground state of the Rydberg model. (b): Phase diagram of the Robustness of Magic \mathcal{R} for the ground state of the Rydberg model. Simulations were performed for $N = 51$ atom and we set $\Omega = 1$ and vary Δ and V . Due to the large van der Waals decay exponent $\alpha = 6$, we truncate the interactions to next nearest neighbors. The ground state was obtained using DMRG at a bond dimension of $\chi = 4$. The dashed black line represents the path of the effective model H_0 from the main text [61] through the phase diagram, with the cross marking the point of maximal non-stabilizerness ($z \approx 2$) observed in Fig. 1 of the main text.

– a single MPS tensor – are sufficient to reproduce a global quantity, the full SRE. In Fig. S3(c), $m_{\mathcal{I}}^{(2)}$ as defined in the main text, is shown for the full two-site unit-cell ansatz. We see that, despite small deviations, it is significantly closer to the full SRE than either the ROM or 2-site SRE.

Next, we consider the two site reduced density matrix SRE and the robustness of magic for the Rydberg model defined by the Hamiltonian H_{Ryd} in the main text. In Fig.S4(a) we plot the phase diagram of the two-site reduced density matrix SRE for ground state of the Rydberg model. We find this local measure of magic produces an excellent qualitative agreement with the full calculation of the SRE in Fig.2, capturing the large band of non-stabilizerness at $\Delta \approx 0$, and the black dashed line that represents the effective Hamiltonian for the MPS ansatz. The maximal value of the two-site density matrix SRE is $m^{(2)(\rho)} \approx 0.32$, comparable to the actual SRE maximum of $m^{(2)} \approx 0.38$, suggesting tomography would be an effective measure of calculating the SRE. In Fig.S4(b) we plot the phase diagram of the robustness of magic \mathcal{R} for the ground state of the Rydberg model. This measure does not produce much qualitative similarities with the SRE phase diagram in Fig.2, even shifting the band of large SRE towards $\Delta \approx 2.5$. At the point of maximum non-stabilizerness ($z \approx 2$) we actually see quite a low value for \mathcal{R} . However, it should be seen that this metric should not be trusted for studies of quantum many-body systems as it generally cannot accurately reproduce the phase diagram unlike the SRE and does have some issues with convergence. We note that there are a few points at around $V \approx 15$ where the ROM calculation has diverged.

NON-STABILIZERNESS OF EIGENSTATES IN THE PXP MODEL

In the main text we focused on the PXP model and explored the non-stabilizer generated under its constrained quantum dynamics. Here we turn our attention to the non-stabilizer of exact eigenstates of the PXP model. One of the remarkable properties of this model is that it has a few eigenstates in the middle of the energy spectrum that can be written as exact low bond-dimension MPS [52]. This will allow us to directly evaluate their SRE with the replica MPS approach outlined above and in the main text.

First, we analyze two exact scarred eigenstates with energy $E = 0$ exactly in the middle of the spectrum. Assuming even chain lengths and periodic boundary conditions (PBCs), these states were written down in Ref. [52] using the following MPS ansatz:

$$|\psi_1\rangle = \sum_{\{\sigma_i\}} \text{tr}(B_1^{\sigma_1} C_2^{\sigma_2} \dots B_1^{\sigma_{N-1}} C_N^{\sigma_N}) |\sigma_1 \dots \sigma_N\rangle, \quad |\psi_2\rangle = \sum_{\{\sigma_i\}} \text{tr}(C_1^{\sigma_1} B_2^{\sigma_2} \dots C_1^{\sigma_{N-1}} B_N^{\sigma_N}) |\sigma_1 \dots \sigma_N\rangle, \quad (\text{S26})$$

with the MPS matrices given by

$$B^0 = \begin{pmatrix} 1 & 0 & 0 \\ 0 & 1 & 0 \end{pmatrix}, \quad B^1 = \sqrt{2} \begin{pmatrix} 0 & 0 & 0 \\ 1 & 0 & 1 \end{pmatrix}, \quad C^0 = \begin{pmatrix} 0 & -1 \\ 1 & 0 \\ 0 & 0 \end{pmatrix}, \quad C^1 = \sqrt{2} \begin{pmatrix} 1 & 0 \\ 0 & 0 \\ -1 & 0 \end{pmatrix}. \quad (\text{S27})$$

For $|\psi_1\rangle$ and $|\psi_2\rangle$, we find that $m^{(2)} \approx 0.376$, which is significantly larger than, e.g., the SRE at the critical point of the Ising model. However, we find that the SRE of these eigenstates is slightly smaller than maximal SRE we found in the main text.

Apart from the MPS states in Eqs. (S26)-(S27), the majority of PXP eigenstates are believed to be volume-law entangled [41]. Hence, we will rely on Markov chain Monte Carlo sampling to evaluate their SRE. This method overcomes the 4^N scaling of the exact evaluation of the SRE, but it comes at the cost of generally poor convergence with the number of samples required for accurate convergence being $N_s \approx 1 \times 10^6$.

At energy $E = 0$ in the middle of the spectrum, similar to the MPS states in Eqs. (S26)-(S27) above, there are also some volume-law entangled states that can be written down in analytic form. For example, for a spin-1/2 PXP chain with PBCs and size $N = 2L$, where L is the size of the half chain, an exact volume-law entangled eigenstate at energy $E = 0$ is given by the following ‘‘rainbow’’-like state [70]:

$$|E\rangle = \frac{1}{\sqrt{\chi}} \sum_{f \in F_L} (-1)^{|f|} |f\rangle_{1,\dots,L} \otimes |f\rangle_{L+1,\dots,2L} \quad (\text{S28})$$

where F_L is the set of bitstrings for a chain of L spins with PBCs and respecting the Rydberg blockade constraint. The normalization is just the Fibonacci number, $\varphi_n, \chi = |F_L| = \varphi_{L-1} + \varphi_{L+1}$, while $|f|$ denotes the parity of a given bitstring. Performing the Monte Carlo sampling, we computed the SRE of the $|E\rangle$ state for several system sizes L , obtaining the $L \rightarrow \infty$ extrapolated SRE of $m^{(2)} = 0.180 \pm 0.008$. This implies that, in the thermodynamic limit, the $|E\rangle$ state is closer to a stabilizer state compared, e.g., to the peaks in the skeleton model shown in Fig. S1. Intuitively, this may be expected due to the sparse structure of the $|E\rangle$ state when we consider the Hilbert space of the entire $2L$ chain. Additionally, the non-zero amplitudes on basis states in $|E\rangle$ are uniform, requiring fewer non-Clifford gates to construct the state.

Finally, in Fig. S5 we study the SRE of all eigenstates in the PXP model with $N = 14$ spins. We use exact diagonalization (ED) to extract the eigenstates and then apply Monte Carlo sampling to obtain their SRE. Here we assume open boundary conditions (OBCs) while also resolving parity symmetry. We found that OBCs result in a much better convergence of the Monte Carlo sampler compared to PBCs. Fig. S5(a) shows the overlaps of eigenstates with the $|\mathbb{Z}_2\rangle$ state as a function of their energy E , with the color bar showing $m^{(2)}$ of each eigenstate. We also highlight the scarred eigenstates using crosses. The bulk of the spectrum contains a large density of thermal eigenstates with large non-stabilizer. Towards the edges of the spectrum, we see a noticeable drop in $m^{(2)}$, indicating that the ground state and low-energy excitations are closer to stabilizer states.

To isolate the non-stabilizer of the scarred states we plot the SRE of the eigenstate spectrum in Fig. S5(b) and also label the scarred states. The ground state of the spectrum has the lowest SRE of the spectrum with a value comparable to the SRE of the 1D critical Ising model [24, 36]. The scarred eigenstates exhibit a roughly linear increase of SRE until we reach the mid-spectrum eigenstates with the largest overlap on $|\mathbb{Z}_2\rangle$ state. We note that any asymmetry in the plots in Fig. S5 around $E = 0$ is due to accidental degeneracies in the spectrum or convergence issues in Monte Carlo sampling.

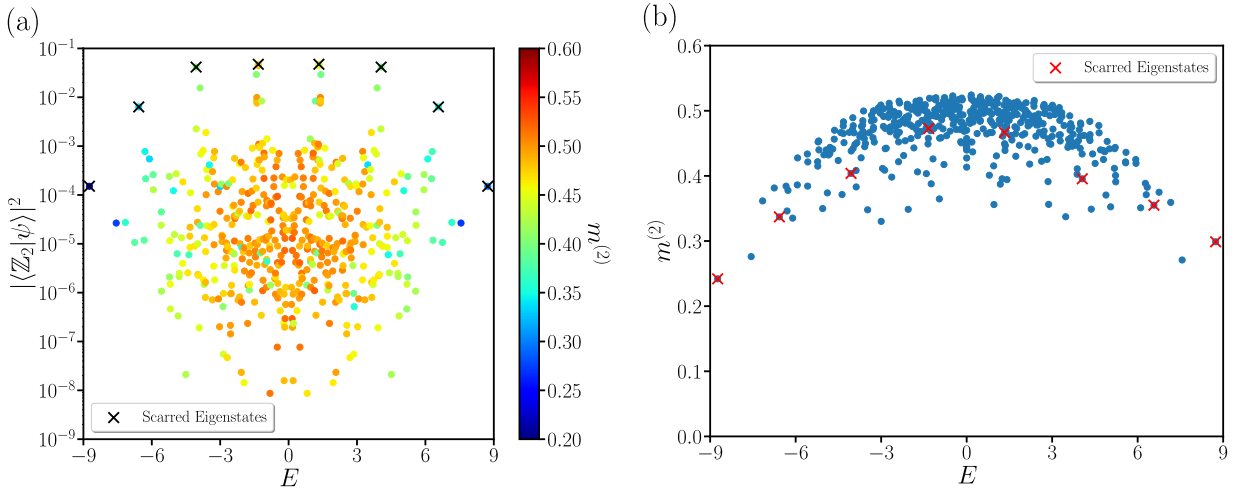


Figure S5. (a) Overlap between the $|\mathbb{Z}_2\rangle$ and all eigenstates of the PXP model plotted as a function of their energy. Each eigenstate is colored by its $m^{(2)}$ value (color bar) obtained by Monte Carlo sampling. (b) SRE of the PXP eigenstates as a function of their energy E . In both panels, the crosses indicate the scarred eigenstates. The simulations were performed for the PXP model with $N = 14$ spins with OBCs and in the $P = +1$ parity sector, using 300000 Monte Carlo samples.